MULTI-DISCIPLINARY OPTIMIZATION OF GYROID TOPOLOGIES FOR A COLD PLATE HEAT EXCHANGER DESIGN

Elhusseiny Daifalla
Industrial Trainee
Innovation Hub, Future Methods,
Rolls-Royce plc, University of Glasgow
Derby, DE24 8BJ, UK
Elhusseiny.Daifalla@Rolls-Royce.com

Shahrokh Shahpar
Rolls-Royce Fellow
Fluid Mechanics Department
Rolls-Royce plc
Derby, DE24 8BJ, UK

Indi Tristanto
CFD Developer
Innovation Hub, Future Methods
Rolls-Royce plc
Derby, DE24 8BJ, UK

Mario Carta
Postdoctoral Research Associate
Fluid Mechanics Department
Rolls-Royce plc
Derby, DE24 8BJ, UK

ABSTRACT

The strive to reduce the environmental impact of aviation hasled to electrification and increasing demand for powerful on- board power electronic systems. These high-performance electrical components are bound to produce significant amountsof low-quality heat waste that, if not dissipated properly, will lead to malfunctioning and even permanent damage. For this reason, high performance heat exchangers represent a key enabler for future advances in aircraft systems electrification and are vital to meet net zero goals and reduce the aviation's carbon footprint. For a given volume of the exchanger, the heatflow rate can be increased by adopting more sophisticated fluid domains. However, excessive geometrical complexity will lead to an increase in pressure losses, often resulting in inhomogeneous temperature distributions. In this paper, a novel optimization procedure is employed to maximize the efficiency of a high- performance heat exchanger, while minimizing overall pressure loss and temperature gradients. The optimization is performed with full-3D high-fidelity computational flow simulations. The geometry of the fluid domain is constituted by triply periodic minimal surfaces, with a parametrization based on thickness and aspect ratios, done by using the nTopology suite. To assess the performance gain, the topology-optimized design is compared against the datum case and a conventional serpentine design.

INTRODUCTION

Heat management is currently a topic of great scientific and industrial interest. This is due to the continuous electrification process, which poses the problem of being able to manage the copious amounts of excess heat produced by modern high-power electrical systems. In this field, topology optimization is a powerful tool that can provide effective design solutions to maximize heat transfer. In particular, numerous studies started investigating the potential thermal performance improvements of novel Triply Periodic Minimal Surfaces (TPMS) designs. In 2021, Kaur and Singh [1] investigated the convective heat transfer numerically in two TPMS sheet-based structures and compared it to commercially available metal foam structures, with the gyroid structure exhibiting improved average heat transfer coefficient in addition to higher pressure drop per unit length. Kaur also advocated for comprehensive CHT modelling to fully realize the benefits of the TPMS designs. Another recent study by Li et al. [2], analyzed two heat exchanger (HX) designs, adopting the Gyroid and Schwarz-D TPMS cells, numerically at Reynolds numbers ranging from 2,300 to 70,000. Benchmarked against a reference printed circuit heat exchanger (PCHE), the TPMS designs achieved a 15-100% thermal performance improvement for the given pumping power. Attarzadeh [3] developed a CHT CFD model testing 4 TPMS based HX designs with varying cell thickness and fluid velocities. The study demonstrated the significant impact of the TPMS cell thickness on the thermal performance as well as the advantages of incorporating such TPMS structures in novel HX. A study published in 2023 by Alteneiji [4] presented the numerical results of sectioned TPMS lattices in a crossflow HX at varying flow rates. In line with other studies, the results favored the Gyroid design in terms of thermal performance and effectiveness, ε. Manufacturability of HX with such complex geometry can be an issue. Recent experimental studies, such as the ones by Femmer [5] in 2015 and Dixit [6] in 2022, opted to print TPMS HX prototypes using commercially available resin and tested for low Reynolds number applications (10–40). These studies along with advances in additive manufacturing paved the way for further investigation of setups more suitable for aerospace and industrial applications. In 2023, Liang [7] tested 3 HX at relatively high Reynolds

numbers ranging from 2300 to 8900. These cases were printed in aluminum alloy powder using Selective Laser Melting (SLM). Mahmoud [8] employed laser powder bed fusion (LPBF) to make 5 HX with varying lattice structures out of AlSi10Mg. It should be noted that Peng's [9] metal TPMS HX prototype, made also using the EOS M290, failed the leakage test with wall thicknesses of 0.2 mm. These studies helped give a more comprehensive understanding of the manufacturability of TPMS structures, limitations of their respective methods, as well as highlighted the potential performance improvements of integrating TPMS lattices in novel HX while presenting the discrepancy between CFD and experimental results. This study investigates the use of non-uniform gyroid TPMS lattices in novel cold plate designs in such a way that promotes heat transfer by increasing turbulence mixing and maximizing the solid-fluid interface surface area. By using these lattices, the fluid forms a single U-bend topology made up of multiple interconnected entangled channels that induce secondary flows throughout the entire fluid domain. Optimizing the geometric features of these gyroid lattices and their subsequent effect on the size and number of the fluid channels can then further enhance the thermal performance of the HX. This often comes at the expense of higher pressure losses making it essential to balance the improved performance versus the increased pumping cost. It is also important to maintain flow uniformity as it ensures surface temperature uniformity of the heat cells (HC). To find this balance, the gyroid lattice structure is parametrized using nTopology [10] into eleven parameters that control the gyroid unit cell aspect ratio and thickness variation across the fluid domain. These parameters are then optimized using a Multi-Objective (MO) Design of Experiments (DoE) [11] approach to find the optimal configuration for the gyroid lattice. The optimization relies on simulating the full domain in Ansys Fluent 2021R2 [12] using high fidelity CHT CFD. The Krig Estimated Improvement (EI) surrogate model will then iterate the DoE by predicting optimum configurations based on the four objective functions. The objective functions are overall heat transfer coefficient, average HC temperature, maximum HC temperature difference, and total pressure drop. The objective functions are further discussed in section 2. Early results show that for a uniform (unoptimized) gyroid latticed cold plate, the fluid flows directly from inlet to outlet taking the path of the least resistance thus leaving the rest of the HX starved of cooling. This parametric optimization also addresses such undesirable flow behavior as geometric changes to the gyroid lattice change the channel flow resistance minimizing pressure loss. After reaching a converged pareto front (PF) representing the optimum designs for the nTopology model, a performance-focused comparative study will be presented ranking the designs in terms of effective heat transfer, surface temperature differences, and relative reductions in pressure loss to find the optimal design and approach. Although recent literature findings encourage further investigation of TPMS HX designs, the authors focus their numerical thermal analysis on a regular array of TPMS cells or a section of the intended lattice with a uniform distribution of the cell properties. This sectioned setup can also be seen in 3D topology optimization studies to keep the computational demand manageable as done by Marshall and Lee [13]. To the author's knowledge, there have been no published technical studies that modelled the entire HX to perform CHT CFD or attempted to

further optimize the fluid domain by varying the TPMS cell porosity and aspect ratio over the fluid domain.

METHODOLOGY

To establish fundamental indicators of the HX performance that can be used as objective functions for the optimization, we need to consider the heat transfer rate Q defined by Equation (1) and the increased pumping power cost $W\ pump$ defined in Equation (2).

$$\dot{Q} = UA(T_{avg} - T_{in}) \quad (1)$$

where U is the overall surface heat transfer coefficient, A is the total effective solid-fluid interface area, T_{avg} is the average temperature, and T_{in} is the inlet coolant temperature. U encompasses heat transfer due to molecular diffusion as well as convective mixing, including secondary flows. As such, increased turbulence in the flow promotes mixing increasing U across the transition region [14]. As mentioned previously, higher turbulence is achieved by introducing the gyroid lattice to the fluid domain which also increases the solid-fluid interface area and develops secondary flows improving heat transfer rates [15]. To that end, the gyroid wall thickness, which inversely affects the channels' width, is then optimized to adjust the fluid channel resistances. Other geometric adjustments such as higher surface roughness will also affect both U and A by increasing mixing as well as effective mixing area. Due to this coupled nature, UA is often taken together and will be referred to as effective heat transfer.

$$\dot{W}_{pump} = VA_{in}\Delta P \quad (2)$$

where V is the inlet velocity, A_{in} is the inlet area, and ΔP is the total pressure difference between inlet and outlet. The cost of inducing secondary flows is increased pressure loss and friction losses [14]. Since increased flow channel resistance requires higher pumping power, there is a case to find an optimal balance between thermal and pressure performance. This ensures the coolant does not stagnate, hindering the component's performance. Holman [15] also references Bergles' [16] investigation of the importance of pressure drops and pumping cost in HX design. Therefore, the resulting characteristics of the fluid channels will have significant impacts on the HX's cooling capability, temperature uniformity, and pumping cost. In this case, increased pumping power equates to the cost associated with optimizing the HX.

Cold Plate Heat Exchanger

A cold plate heat exchanger is used as a heat sink for power electronic devices. The plate temperature is managed by transferring heat into coolant fluid. Therefore, for modelling purposes, the power electronic devices can be treated as heat sources to be conducted onto the fluid interface, which will then convect the heat away. Fig. 1 shows the baseline geometry with the flow inlet and outlet on the same side and 3 power

electronic chips on each surface (6 HC in total). Cold plates usually have additional requirements to ordinary heat exchangers, namely to maintain the surface contact temperature with the HC to be within tolerances of the power electronics. Hence, uniform temperature across all HC is paramount. A multi-pass serpentine cooling channel with 180° U bends is commonly used to meet this temperature distribution requirement. However, the bend generally leads to high pressure loss due to secondary flow with only limited heat transfer benefit. In this work, UA and the average HC temperature are used as optimization objectives 1 and 2 respectively to evaluate the overall HX thermal performance. To ensure temperature uniformity across the surface of the HX, the maximum temperature difference of the 3rd HC (HC3), which is furthest from the inlet and exhibits the widest temperature range, is taken as objective 3. For ideal reversible processes, $Wpump$ has to be zero. Therefore, ΔP is minimized as objective 4 to minimize the optimization power cost. All 4 optimization objectives are summarized in Table 1. No objective function weighting or constraints have been applied prior to the optimization. Other quantities useful in evaluating the HX performance and thermal profile are efficiency, Reynolds range of the flow, and area density. Using Equations (1) and (2), we can define efficiency.

$$Efficiency\ (\%) = [\dot{Q}/(\dot{Q} + Wpump)]\cdot 100 \quad (3)$$

Equation (3) is assumed for a constant inlet coolant temperature as it does not account for power required to cool the fluid further. The representative bulk Reynolds number indicates the flow regime in the HX. The characteristic length used for the TPMS designs is the hydraulic diameter of the inlet ($Dh = 4\times A_{in}/Perimeter$), while the inlet velocity is calculated using Equation (4). The density and viscosity values of the fluid are reported in Table 6.

$$V = \dot{m}/(\rho in Ain) \quad (4)$$

where $\dot{m}$ is the coolant mass flow rate and ρ is the coolant density at the inlet. Another method to express effective heat transfer area A non-dimensionally is in terms of area per unit volume (i.e., area density). Area density is useful to compare the degree of utilization of HX of different sizes and can also be used to define the HX weight given specific material properties.

$$Area\ Density = A/(Total\ Volume) \quad (5)$$

Optimization Strategy

The optimization workflow, summarized in Fig. 2, is articulated in five stages dedicated to geometry generation and assembly, meshing, CFD simulation, and surrogate model updating. For each DoE run, a new solid-fluid interface is created with the corresponding set of design parameters and imported into BOXER mesh [17], replacing the older interface, for automatic meshing. The updated mesh is then passed on to the CFD solver and the CHT simulation is conducted, providing the new performance metrics. The optimization is performed using Optimat [18] utilizing the Kriging

Response Surface Method (RSM) surrogate model while the multi-objective algorithm is an improved implementation of NSGA2 [19]. The surrogate model has had three iterations with a total of 38 successful runs. The first iteration (i.e., the initial DoE), aimed at exploring the design space, consisted of 25 points generated using the Soton Optimal Latin Hypercube. The following iterations had points aimed to continually explore the design space based on the Expected Improvements (EI) [19] model while the rest was dedicated to improving the predicted pareto front.

Geometry and parameterization

The cold plate overall dimension is maintained throughout the optimization process. However, the gyroid designs have a 20x8 mm square inlet, resulting in a hydraulic diameter of 11.4 mm, compared to the baseline serpentine which has a 6 mm diameter circular inlet. The gyroid designs have a larger inlet to ensure multiple channels are connected directly to the inlet. This allows a wider range for the gyroid cell sizes as larger cells could have blocked a majority of the smaller inlet design. Furthermore, the outlet has been extended to eliminate reverse flow. The thickness of the gyroid and fluid regions is 8 mm while the total thickness of the HX is 12 mm. The full geometry assembly of the gyroid TPMS designs is shown in Fig. 3. The HX has a novel fluid domain design that features a gyroid lattice with varying TPMS cell aspect ratio and thickness. The variation is controlled by parameters that aim to fine tune the fluid channel resistance to produce the desired thermal and pressure profiles. An initial workspace is developed in nTopology focused on producing a uniformly latticed TPMS HX. This workspace was then iterated multiple times to optimize the lattice structure, parameterize the workspace, and address any errors that appear throughout the process. The nTopology workspace starts by defining the Solid and fluid domains shown in Fig. 4. A gyroid lattice structure is then created within the defined boundaries and trimmed to remove any excess as shown in Fig. 5. This is then followed by Boolean operations to subtract the fluid from the solid lattice and merge it with the inlet and outlet. Eleven parameters in this workspace were then selected to be optimized, based on the DoE methodology defined in section 2.1, to produce multiple optimum designs from the pareto fronts. The 11 optimization parameters (P1-11) selected can be split into two groups. The first group is dedicated to controlling the TMPS cell sizes and scaling in the x-direction while the second group controls the thickness variation across the gyroid lattice. The parameters pertaining to the first and second groups are reported in Tables 2 and 3 respectively. To generate the gyroid lattice, P1 and P2 are used to control the gyroid cell sizes which conversely set the number of gyroids in the lattice in the X and Y directions, respectively. P3 then enlarges the x-axis cell size (P1) so that cells far from the inlet side are elongated. The resultant gyroid lattices for the lower and upper limits of P1 are shown in Fig. 6 (a) and (b) respectively. As seen, group 1 parameters control the number of fluid channels in the horizontal and vertical directions independently as well as the horizontal elongation of the channels. Group 2 specifies the range of thickness variation and the distribution field. The range is controlled by P4 and P5 while the distribution field is the result of combining three separate planes, each with a defined origin point and orientation. Each of the planes creates a uniform field in the XY plane as in Fig. 7 (a)– (c). Combining the 3 planes with

a scaled rounding value produces the combined distribution field shown in Fig. 7 (d). Fig. 7 (e) is the thickness variation plane that is simply a scaled version of Fig. 7 (d) to fit within the specified thickness range. The final resulting geometry of the thickness variation described in previous paragraph is in Fig. 8 (a), which is aimed to minimize the pressure loss by having a single primary U-bend topology annotated by the arrows. However, the nature of the TPMS geometry results is multiple branches to be created between the primary legs of the U-bend. As a result, the flow might choose the path of least resistance that connects the inlet and outlet without going to the far end where HC3 is located. Thus, the limits allowed for these parameters can produce a wide range of thickness variation fields that can direct the coolant flow by altering the channel resistance. Fig. 8 (b) is an example of a different set of parameter values to highlight the possible geometries of this design space. With the solid-fluid interface exported from nTopology along with the inlet and outlet, the geometry for the six HC and the outer solid is set up in SpaceClaim [20]. The full geometry is then inspected using SpaceClaim's 'Detect' functions to ensure it is sufficiently 'watertight' for Boxer to mesh the regions correctly.

CFD Mesh and Solving Technique

When modelling HX for flow simulation, it is recommended that the meshes have 10-15 elements across the boundary layer thickness, a mesh expansion ratio ≤ 1.2-1.3, and a Y+ ≈ 1. The meshes should ideally be conformal with minimum orthogonal quality ≥ 0.01, have low skewness, and moderate aspect ratio. These guidelines aim to minimize the discretization error when running CFD simulations [21]. Iteration errors can also affect the results significantly. Therefore, the mass flow rate and heat transfer rate fluxes are monitored, alongside the residuals, making sure that their net values are orders of magnitude smaller than the model values. Papukchiev [22] argued that CHT modelling is necessary for accurate results by assessing the deviation between numerical and experimental results. In an attempt to simulate this complex fluid domain fully to the standards set above, different mesh resolutions for the gyroid datum design were evaluated ranging from 55.6 M to 99.2 M, Table 4. For the purposes of this study, the 85.5 M configuration, shown in Fig. 9, was deemed to provide sufficient resolution as the percentage difference in pressure drop compared to the 99.3 mesh configuration is ≈ 0.72%. As the gyroid lattice is a construct of exact mathematical equations, nTopology's implicit body representation will capture sharp and thin features at a resolution that is higher than that of the CFD mesh. This causes issues when exporting the fluid interface as CAD from nTopology as well as when meshing it in Boxer as it leads to the collapse of prism layers near sharp angles. This has also been observed in meshes produced by fluent mesh. To ensure good quality meshes, these features must be removed using a defeaturing (rounding) operation in nTopology that matches the underlying resolution of the CAD to the resultant mesh in Boxer. This process filters features approximately smaller than 0.55 mm while limiting the deviations from the original geometry to less than 0.275 mm. A requirement of the defeaturing operation is to have a sufficient tolerance difference between the smallest wanted features and the biggest unwanted features which is accounted for in the P4

and P5 limits. The result of this process can be seen in the rounded corners of Fig. 9 (b). Table 5 details the CFD setup models while Table 6 summarizes the boundary conditions implemented. Considering the size of each individual mesh of the DoE (80+ million cells) and the significant computational resources and time each CFD simulation required, the effect of partial convergence on the objective functions was investigated. A trial CFD simulation was run for 1000 iterations and the values of the 4 objective functions were compared at 300, 500, and 1000 iterations as shown in Table 7. The objectives show a limit-cycle behavior after 300 iterations with minimal changes thereafter. Therefore, partial convergence to 300 iterations was deemed sufficient.

RESULTS AND DISCUSSION

The performance changes shown for the TPMS designs can be attributed to either the use of gyroid lattices or the parametric optimization. The first can be identified by comparing the datum design (i.e., no scaling or thickness variation with mid-range cell sizes) to the baseline serpentine while the latter is highlighted by comparing the optimum designs to the datum. The three most optimum designs are chosen from the CFD based PF shown in Fig. 10. The designs were chosen based on having the best thermal and pressure performance as well as the best balance between the two. The predicted PFs in Fig. 11 (b) and (d) show the predicted thermal and pressure limits of the system dictated by the boundary conditions, mainly inlet coolant temperature and mass flow rate. The PFs also highlight the relation between each of the objective functions. As expected, improvements in pressure drop incur a cost as a reduction to UA and the temperature objectives (O2 and O3) and vice versa. The temperature objectives seem to vary linearly with UA. By comparing the predicted PF to the CFD based PF, Fig. 11 (a) and (c), we can validate Optimat's predictions and identify the possible performance improvements with further iterations. Fig. 12 (a)-(d) show the final iteration cell maps for each objective and how it varies with P1 and P2. As these cell maps continue to evolve with each iteration increasing the resolution, they show how the objectives vary across the design space and highlight areas of interest to explore. Furthermore, the surrogate model is able to better distinguish the local and global minima in the design space with each iteration. Starting from the 3rd iteration, the design space was expanded by extending the parameter limits by ±5%. This expansion yielded improved results indicating additional expansion of the design space could improve the optimum designs further. The best five thermally performing DoE points all featured a higher gyroid cell thickness around the inlet adjacent region as well as a cell aspect ratio (P1/P2) of 2.4-2.6 meaning the channels were relatively elongated in the x-axis. On the other hand, designs with a lower aspect ratio (1.7-2.3) have lower pressure drop values. This behavior is similar to conventional cold plate HX where increasing the number of channels improves heat transfer and temperature uniformity while having wider channels reduces pressure loss. Pressure profiles are highly affected by the inlet-outlet dimensions and the fluid region surrounding them at the beginning of the gyroid lattice. As the serpentine geometry has different inlet-outlet dimensions and shape, direct comparison to the gyroid designs would not be accurate without investigating and accounting for that discrepancy. Therefore,

pressure drop for the optimum designs is benchmarked against the datum case to isolate the effect of the gyroid lattice optimization on the pressure profile. For direct comparison to the serpentine, efficiency, Equation (3), is used as the cost is expressed in terms of relative increase in pumping power. The datum geometry has a pressure drop of 1165.8 Pa. As a result of the optimization, the PF points have pressure drops ranging from 448.74 Pa (≈61.5% reduction) to 1370.9 Pa (≈17.6% increase). By inspecting the three most optimum designs we can identify key characteristics of the gyroid lattice and their effect on the results. This can then be used to tailor the performance of these novel HX to the specific system requirements. In Table 8 and as shown in Fig. 10, Opt.1 maintains the best thermal performance, Opt.2 has the lowest pressure drop, and Opt.3 is a compromise between the two. To understand why Opt.1 exhibits the best thermal performance with effective heat transfer (UA) 6.84% higher than the serpentine, we compare the temperature and velocity contours of Opt.1 and Opt.2, in Fig. 13 and (b) respectively. The resulting gyroid creates two distinct paths at different cross-sectional heights that are interconnected inwards and outwards of the XY plane. Some Cross-sectional slices exhibit vertical paths that transfer the fluid from the inlet side (bottom side) to the outlet side (top side), as shown at the top of Fig. 13. Other cross-sectional slices exhibit horizontal fluid transfer to the far end of the plate, as shown at the second row of Fig. 13. The resulting flow paths produce a veins network that is equivalent to that of parallel circuit U-bend. The paths that are closest to the inlet and outlet can be considered as main veins of the HX. As mentioned earlier, unoptimized gyroid designs, such as the datum design, show poor temperature uniformity. This is due to having wide enough vertical paths that most of the fluid simply goes from inlet to outlet without fully circulating through the rest of the fluid domain. Designs that have a higher aspect ratio such as in Opt.1, have more horizontal paths and fewer vertical paths compared to the datum. This is in addition to the higher minimum gyroid cell thickness resulting in narrower fluid channels and increased flow velocity. These characteristics force the fewer, narrower vertical paths near the inlet to become congested, forcing the cooler fluid to reach further into the HX before moving to the outlet side improving the thermal performance especially for HC3. This is proven by the Opt.1 contours having lower HC3 temperatures and higher flow velocity in the rightmost vertical paths. However, the optimization of the fluid channels has to be balanced to avoid negative effects on the pressure and temperature distributions. Fine-tuning the aspect ratio and thickness variation can yield further performance improvements. To optimize for pressure drop as in Opt.2, gyroid designs require wider, elongated channels so the lattice is made up of fewer, larger gyroid cells. Opt.3 presents a compromise between both designs by having a relatively high aspect ratio and low minimum gyroid thickness. For the conventional serpentine, reductions in fluid velocity and subsequent increases in pressure drop occur with every turn. Meanwhile, the optimum designs have a significant increase in velocity immediately after the inlet region which gradually dissipates as the fluid fills all the branching channels. Unique to the gyroid designs, the fluid velocity starts to increase again near the outlet as the flow from multiple channels starts to converge. We also notice significant secondary flows spread throughout the entire fluid domain, which aids in

heat transfer across the transition regions, even though the flow is transitional for the gyroid designs based on the bulk Reynolds number. This highlights the main benefit of gyroid TPMS designs, which is the presence of multiple interconnected fluid channels, as the entire domain exhibits the desirable heat transfer behavior of serpentine turns without the significant pressure drop and velocity reduction associated with them. The optimum designs maximize the interface area for a constant volume and display a much higher efficiency than the serpentine reflecting the reduced relative pumping power cost. A robustness study was conducted to assess the adaptability of the optimum designs to changing boundary conditions and its effect on the efficiency to meet specific design goals, Table 9. When compared to the serpentine, the datum exhibits a wider temperature range with higher temperature gradients. This is improved for the optimum designs by up to an approximate 40.1% reduction in ΔT compared to the datum. Increasing the inlet mass flow rate for Opt.1 produced comparable uniformity and improved surface temperature to the serpentine at a lower flow rate. Although this incurs nearly 3.36 times more pressure loss, it results in comparable efficiency indicating an equivalent relative cost to the serpentine with a lower flow rate making it necessary to consider the trade-offs based on system requirements. Applying a higher flow rate to the serpentine resulted in extremely low efficiency reflecting the much higher pumping power needed to meet this boundary condition. Unsurprisingly, changing the coolant temperature for Opt.1 yields improvements in the average HC temperature without affecting the pressure ranges or temperature uniformity but comes at the cost of higher cooling power. Based on the results shown in Table 9, more comprehensive parametric optimizations should include boundary conditions such as mass flow rate and inlet coolant temperature as optimization parameters. Adjusting those values could enhance the thermal performance of the optimum pressure designs creating more efficient solutions. The pressure contours for Opt.1 and Opt.2, Fig. 14, show expected results with a major reduction in pressure in the inlet adjacent region followed by gradual decreases over the rest of the fluid domain. An interesting observation in Opt.1, that is not as noticeable in Opt.2, is the pressure discrepancy between adjacent horizontal paths which gradually fades closer to the outlet side. This is dependent on how well connected the path is to the inlet and suggests the width of the inlet design and flow channels will also affect the local pressure distribution even past the inlet starting region.

CONCLUSION

In this study, a novel TPMS HX design was parameterized and optimized successfully using DoE-based optimization methodology utilizing full domain high fidelity conjugate heat transfer CFD simulations. The optimum designs offer a 6.84% increase in effective heat transfer as well as an efficiency that is approximately 35-41% higher when compared to the serpentine. The optimization of the gyroid lattice has reduced the pressure loss by 61.5% compared to the datum. The optimum thermal design has reduced the average temperature of the heat cells by 2.8K at a much higher efficiency compared to a serpentine design. By adjusting the mass flow rate, the optimum design

was able to produce temperatures lower by 8.73K at a comparable efficiency to the serpentine. Since the TPMS HX features significantly higher effective heat transfer surface areas, accounting for surface roughness in future work will further increase the performance difference when compared to the conventional serpentine. The results prove that TPMS utilization in thermal applications can be fine-tuned to yield significant surface temperature reduction while maintaining the desired pressure and temperature uniformity profiles.

ACKNOWLEDGEMENTS

The authors would like to acknowledge Rolls-Royce plc for their support and permission to publish this work. This work has been conducted within the framework of the NEXTAIR project and funded by the UK Research and Innovation (UKRI) under the UK government's Horizon Europe funding guarantee No. 10038896. The authors would like to thank Dr. Ivan Voutchkov for his valuable help operating the Optimat code.

NOMENCLATURE

A	Total effective solid-fluid interface area
A_{in}	Inlet surface area
Cp	Specific heat capacity
$\dot{m}$	Mass flow rate
ΔP	Total pressure drop from inlet to outlet
A	Total effective solid-fluid interface area
Ain	Inlet surface area
Cp	Specific heat capacity
$\dot{m}$	Mass flow rate
ΔP	Total pressure drop from inlet to outlet
$\dot{Q}$	Heat transfer rate
$Tavg$	Average heat cells temperature
Tin	Inlet coolant temperature
ΔT	Temperature difference for HC3
U	Total heat transfer coefficient
V	Inlet Velocity
$Wpump$	Pumping power
DoE	Design of Experiments
HC	Heat cell(s)
HC3	3rd heat cell, furthest from inlet
HX	Heat Exchanger
MO	Multi-objective
O1-4	Objective functions 1 to 4
P1-11	Optimization Parameters 1 to 11
PF	Pareto Front
TPMS	Triply Periodic Minimal Surfaces

$\dot{Q}$	Heat transfer rate
T_{avg}	Average heat cells temperature
T_{in}	Inlet coolant temperature
ΔT	Temperature difference for HC3
U	Total heat transfer coefficient
V	Inlet Velocity
W_{pump}	Pumping power
DoE	Design of Experiments
HC	Heat cell(s)
HC3	3rd heat cell, furthest from inlet
HX	Heat Exchanger
MO	Multi-objective
O1-4	Objective functions 1 to 4
P1-11	Optimization Parameters 1 to 11
PF	Pareto Front
TPMS	Triply Periodic Minimal Surfaces

REFERENCES

[1] I. Kaur and P. Singh, "Flow and thermal transport characteristics of Triply-Periodic Minimal Surface (TPMS)-based gyroid and Schwarz-P cellular materials," Numerical Heat Transfer Part A: Applications, vol. 79, no. 8, pp. 553-569, 2021.

[2] W. Li, G. Yu and Z. Yu, "Bioinspired heat exchangers based on triply periodic minimal surfaces for supercritical CO2 cycles," Applied Thermal Engineering, vol. 179, 2020.

[3] R. Attarzadeh, M. Rovira and C. Duwig, "Design analysis of the “Schwartz D” based heat exchanger: A numerical study," International Journal of Heat and Mass Transfer, vol. 177, 2021.

[4] M. Alteneiji, M. I. H. Ali, K. A. Khan and R. K. A. Al-Rub, "Heat transfer effectiveness characteristics maps for additively manufactured TPMS compact heat exchangers," Energy Storage and Saving, vol. 1, pp. 153-161, 2022.

[5] T. Femmer, A. J. Kuehne and M. Wessling, "Estimation of the structure dependent performance of 3-D rapid prototyped membranes," Chemical Engineering Journal, vol. 273, pp. 438-445, 2015.

[6] T. Dixit, E. Al-Hajri, M. C. Paul, P. Nithiarasu and S. Kumar, "High performance, microarchitected, compact heat exchanger enabled by 3D printing," Applied Thermal Engineering, vol. 210, 2022.

[7] D. Liang, C. Shi, W. Li, W. Chen and M. K. Chyu, "Design, flow characteristics and performance evaluation of bioinspired heat exchangers based on triply periodic minimal surfaces," International Journal of Heat and Mass Transfer, vol. 201, 2023.

[8] D. Mahmoud, S. R. S. Tandel, M. Yakout, M. Elbestawi, F. Mattiello, S. Paradiso, C. Ching, M. Zaher and M. Abdelnabi, "Enhancement of heat exchanger performance using additive manufacturing of gyroid lattice structures," The International Journal of Advanced Manufacturing Technology, vol. 126, pp. 4021-4036, 2023.

[9] H. Peng, F. Gao and W. Hu, "Design, Modeling And Characterization Of Triply Periodic Minimal Surface Heat Exchangers With Additive Manufacturing," in Solid Freeform Fabrication Symposium, 2019.
[10] nTopology, "nTopology, Design the future with additive manufacturing," nTopology, [Online]. Available: https://www.ntop.com/. [Accessed 11 12 2023].
[11] S. Shahpar, "Design of Experiment, Screening and Response Surface Modelling to Minimise the Design Cycle Time," in VKI, LS-2004-08, Belgium, 2004.
[12] P. Afonso, "Ansys Fluent 2021 R2 Update," 21 09 2021. [Online]. Available: https://www.ansys.com/content/dam/campaigns/abm/technip/fluent-workflows.pdf. [Accessed 11 12 2023].
[13] S. D. Marshall and P. S. Lee, "3D topology optimisation of liquid-cooled microchannel heat sinks," Thermal Science and Engineering Progress, vol. 33, 2022.
[14] T. L. Bergman, A. S. Lavine, F. P. Incropera and D. P. DeWitt, Introduction to Heta Transfer, Sixth Edition, 2011.
[15] J. P. Holman, Heat Transfer, Tenth Edition, 2009.
[16] A. E. Bergles, "Augmentation of Heat Transfer," in Heat Exchanger Handbook, New York, Begell House, 1998, p. Chap. 2.5.11.
[17] A. A. J. Demargne, R. O. Evans, P. J. Tiller and W. N. Dawes, "Practical and Reliable Mesh Generation for Complex, Real-World Geometries," in AIAA 52nd Aerospace Sciences Meeting, National Harbor, Maryland, USA, 2014.
[18] A. Nasti, I. I. Voutchkov, D. J. J. Toal and A. J. Keane, "Multi-Fidelity Simulation For Secondary Air System Seal Design In Aero Engines," in ASME Turbo Expo, Rotterdam, The Netherlands, 2022, GT2022-80391.
[19] I. Voutchkov and A. Keane, "Multi-objective Optimization Using Surrogates," in Computational Intelligence in Optimization, Applications and Implementations, Springer, 2010, pp. 155-175.
[20] Ansys, "Ansys SpaceClaim 3D Modeling Software," Ansys, [Online]. Available: https://www.ansys.com/products/3d-design/ansys-spaceclaim. [Accessed 11 12 2023].
[21] Ansys, "Best Practices for Mesh Generation - Lesson 2," Ansys, 2023. [Online]. Available: https://courses.ansys.com/index.php/courses/best-practice-guidelines-for-cfd-simulations/lessons/best-practices-for-mesh-generation-lesson-2/. [Accessed 7 12 2023].
[22] A. Papukchiev, D. Grishchenko and P. Kudinov, "On the need for conjugate heat transfer modeling in transient CFD simulations," Nuclear Engineering and Design, vol. 367, 2020.

FIGURE CAPTION LIST

Figure 1: Full Geometry Assemblies in SpaceClaim
Figure 2: Optimization Workflow
Figure 3: Gyroid HX Geometry Assembly in SpaceClaim
Figure 4: Fluid and Solid Domains - The green and red regions combined encompassed the full fluid domain. The added gyroid lattice is limited to the green region.
Figure 5: Trimmed Gyroid Lattice
Figure 6: P1 Lower limit 16.2 mm (a) and upper limit 37.8 mm (b) while P2 = 17 mm

and P3 = 1; yellow color represents the gyroid lattice, blue color represents the subtracted fluid region. This example excludes any thickness variation.
Figure 7: Plane Combination for a Single U-bend Topology
Figure 8: Resulting Lattice Examples
Figure 9: Mesh Representation
Figure 10: Pareto Fronts History
Figure 11: 3rd Iteration Pareto Fronts – UA vs. Pressure drop predicted by optimizer (a) and by CFD (b), UA vs. Delta Temp. predicted by optimizer (c) and by CFD (d)
Figure 12: Objectives Cell map for P1 and P2
The range for P1 and P2 is normalized [0, 1] and includes the 5% design space expansion [-0.05, 1.05].
Figure 13: Temp. and Velocity Contours of Opt.1 (a) & Opt. 2 (b)
Figure 14: Mid-plane Pressure contours of Opt.1 (a) and Opt.2 (b)

TABLE CAPTION LIST
Table 1: Optimization Objective Functions
Table 2: Group 1 Geometric Parameters - Cell Properties
Table 3: Group 2 Geometric Parameters - Thickness Variation
Table 4: Mesh Dependence Study
Table 5: CFD Setup
Table 6: Boundary Conditions
Table 7: Partial Convergence Study
Table 8: Optimum Designs Results Comparison and Parameters
Table 9: Opt.1 Design Robustness

FIGURES

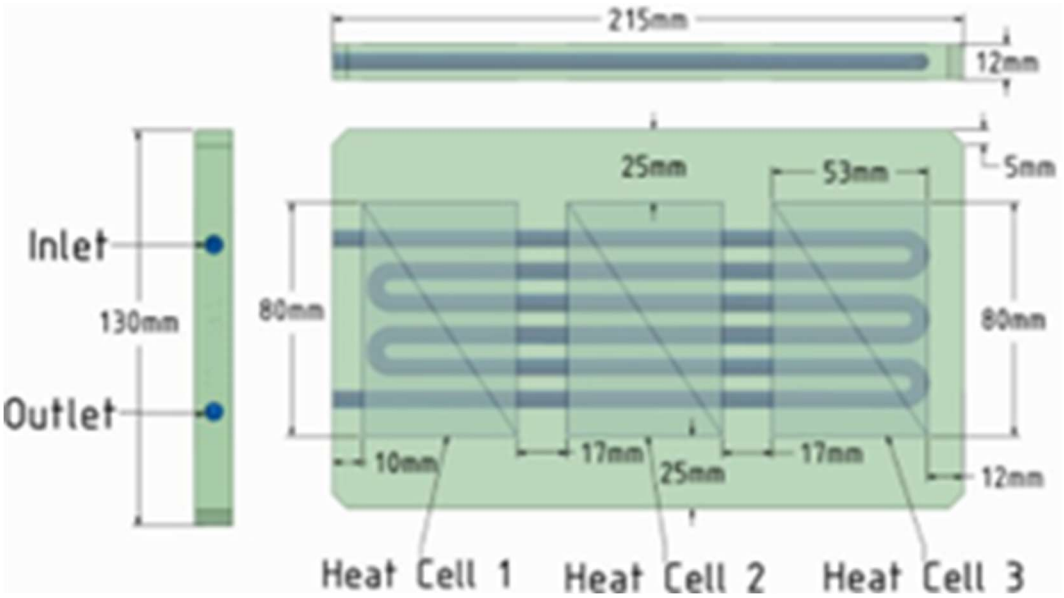

Figure 1: Full Geometry Assemblies in SpaceClaim

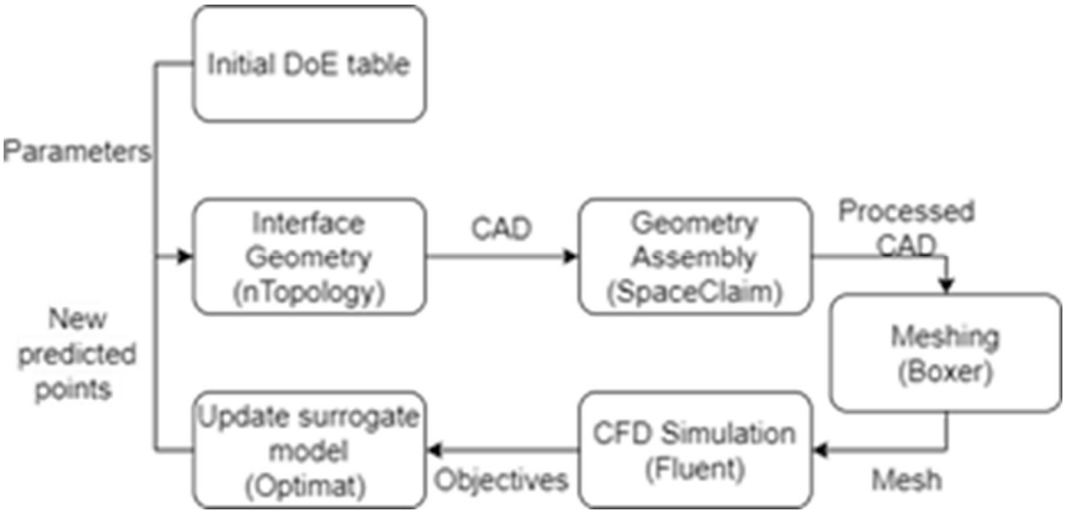

Figure 2: Optimization Workflow

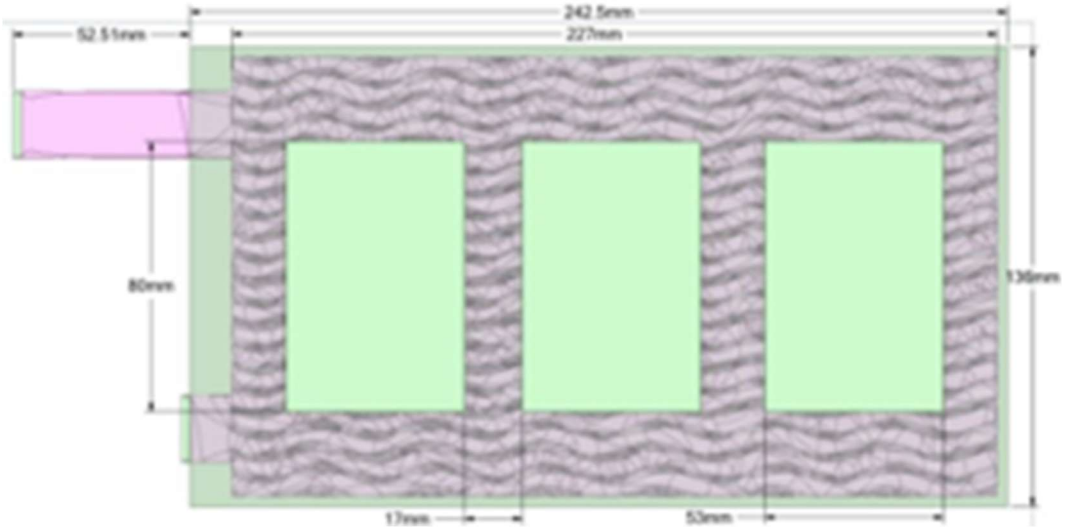

Figure 3: Gyroid HX Geometry Assembly in SpaceClaim

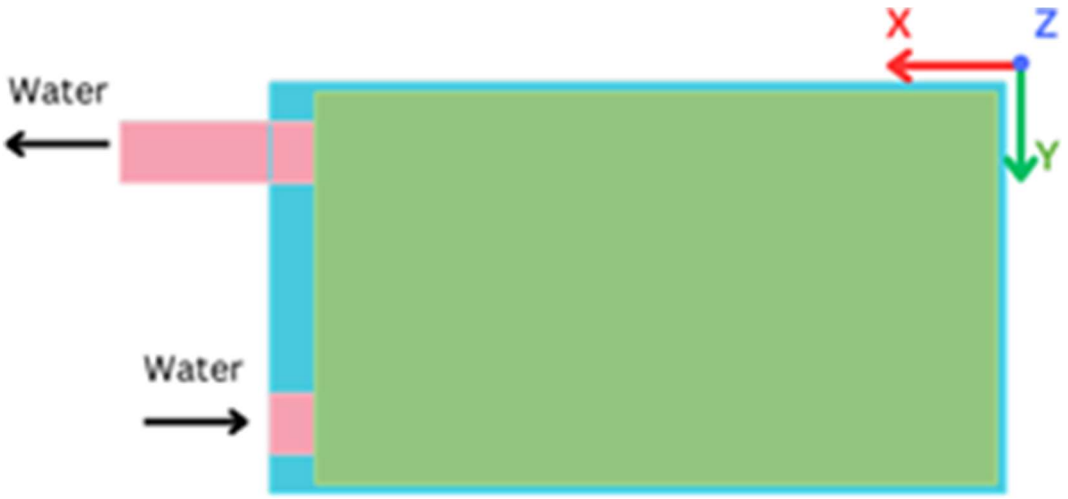

Figure 4: Fluid and Solid Domains - The green and red regions combined encompassed the full fluid domain. The added gyroid lattice is limited to the green region.

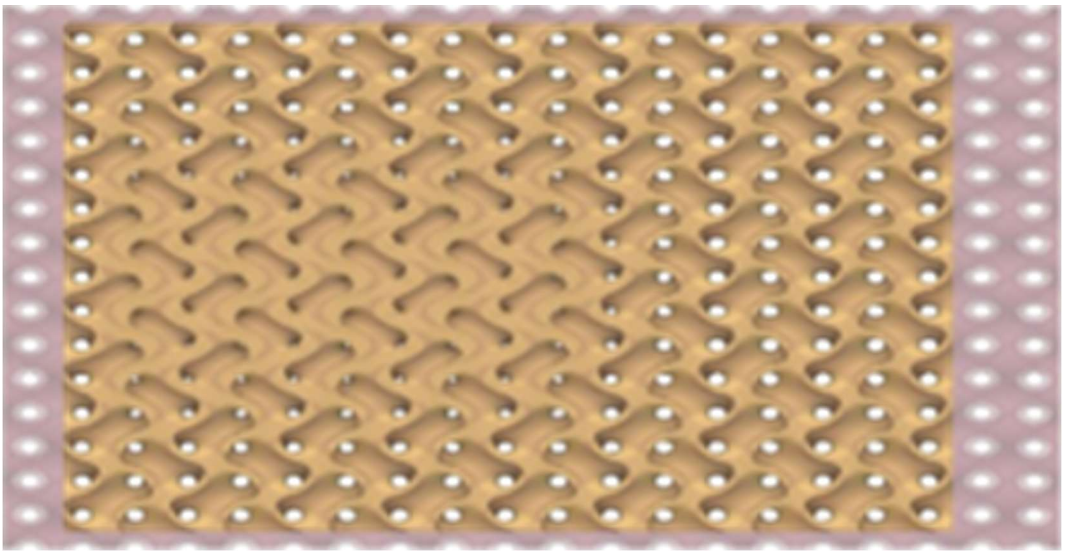
Figure 5: Trimmed Gyroid Lattice

(a)

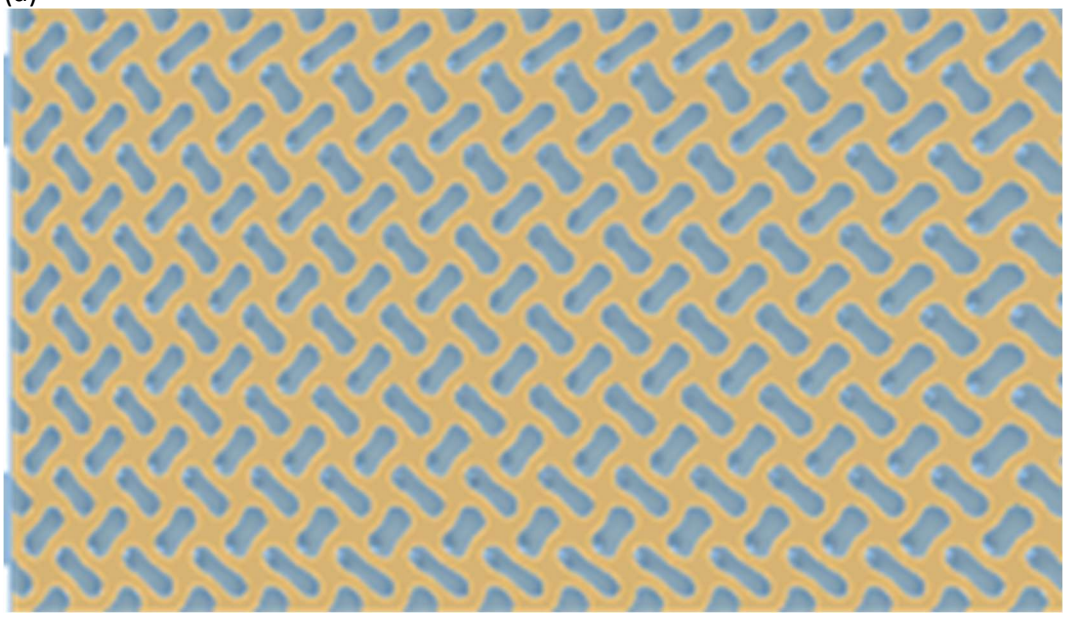

(b)

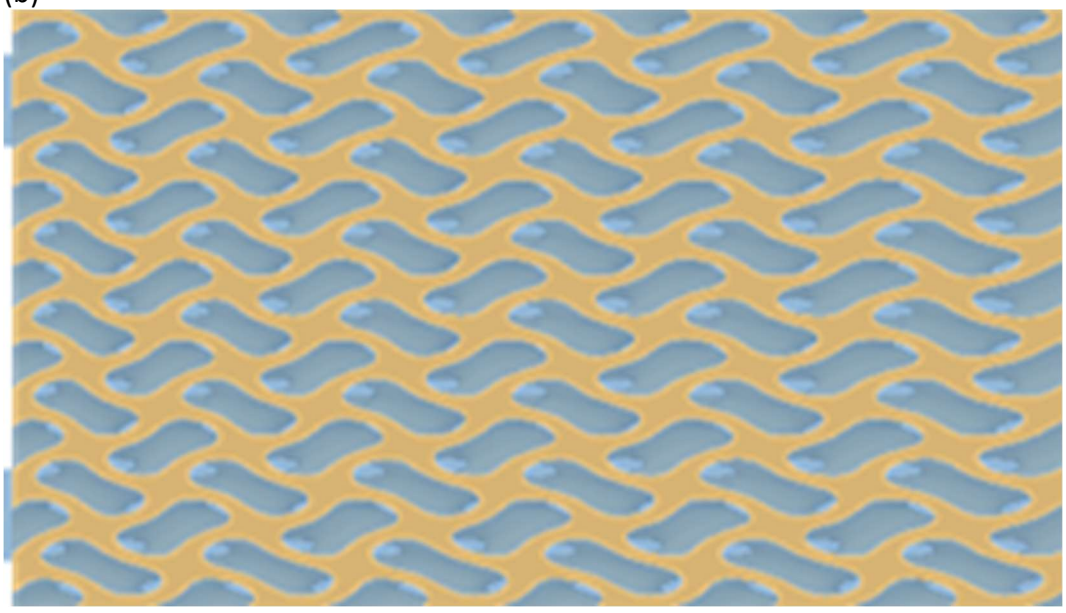

Figure 6: P1 Lower limit 16.2 mm (a) and upper limit 37.8 mm (b) while P2 = 17 mm and P3 = 1; yellow color represents the gyroid lattice, blue color represents the subtracted fluid region. This example excludes any thickness variation.

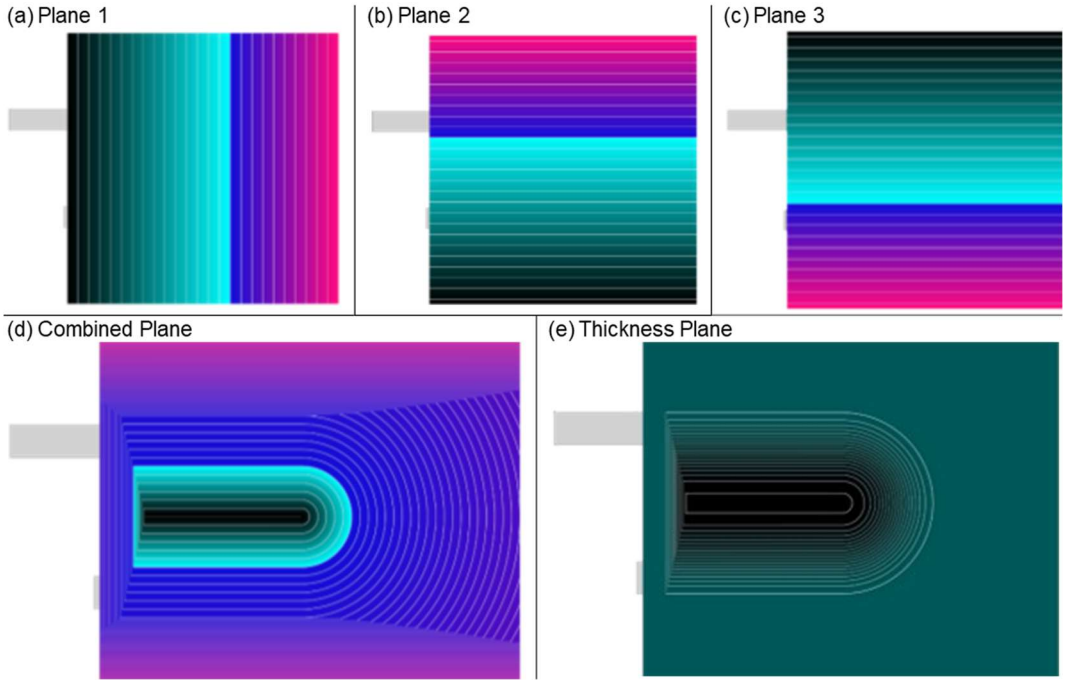

Figure 7: Plane Combination for a Single U-bend Topology

(a)

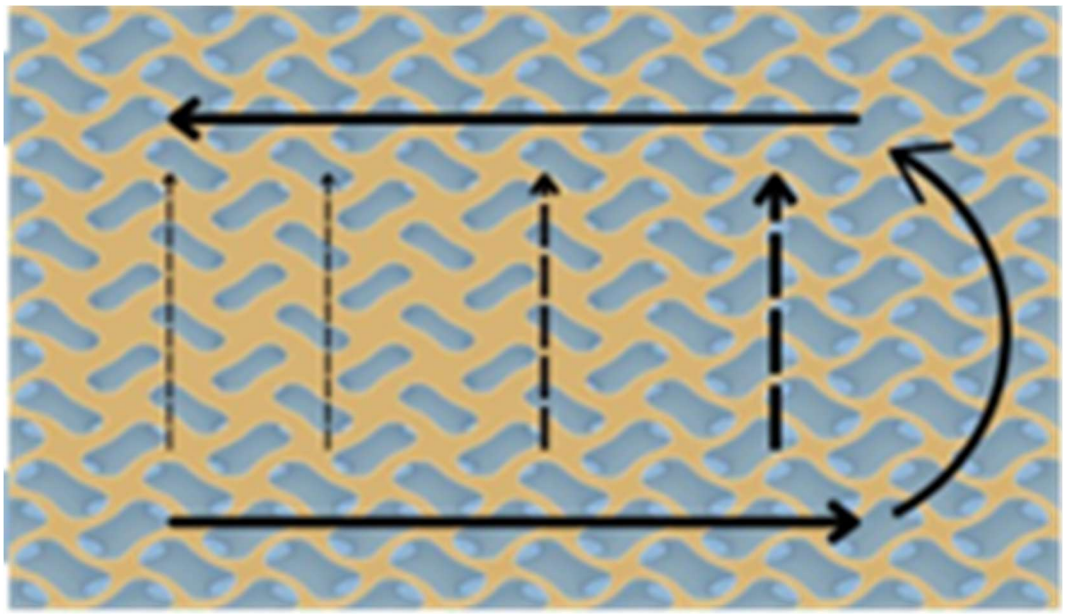

(b)

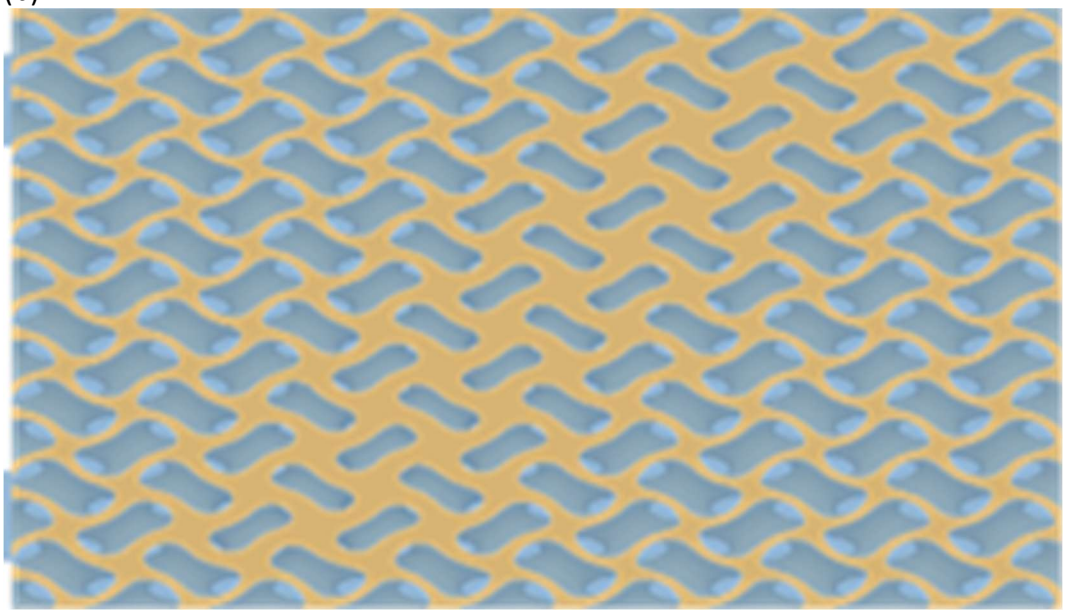

Figure 8: Resulting Lattice Examples

(a)

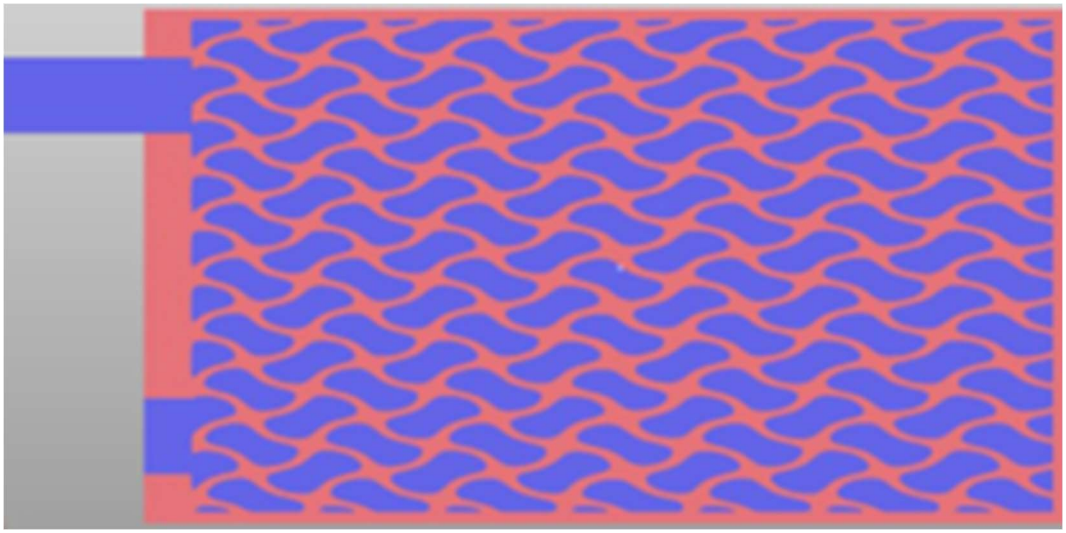

(b)

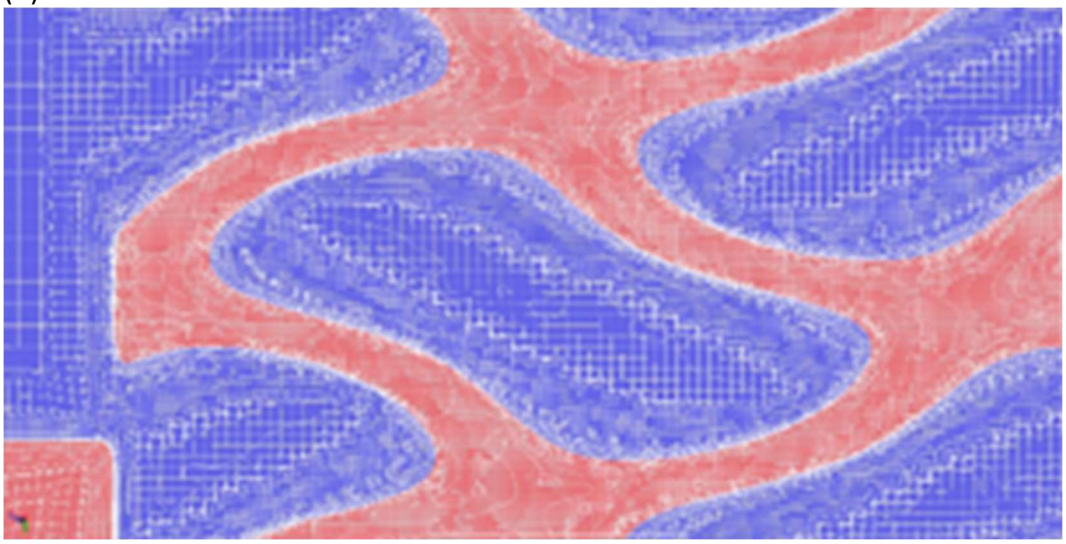

Figure 9: Mesh Representation

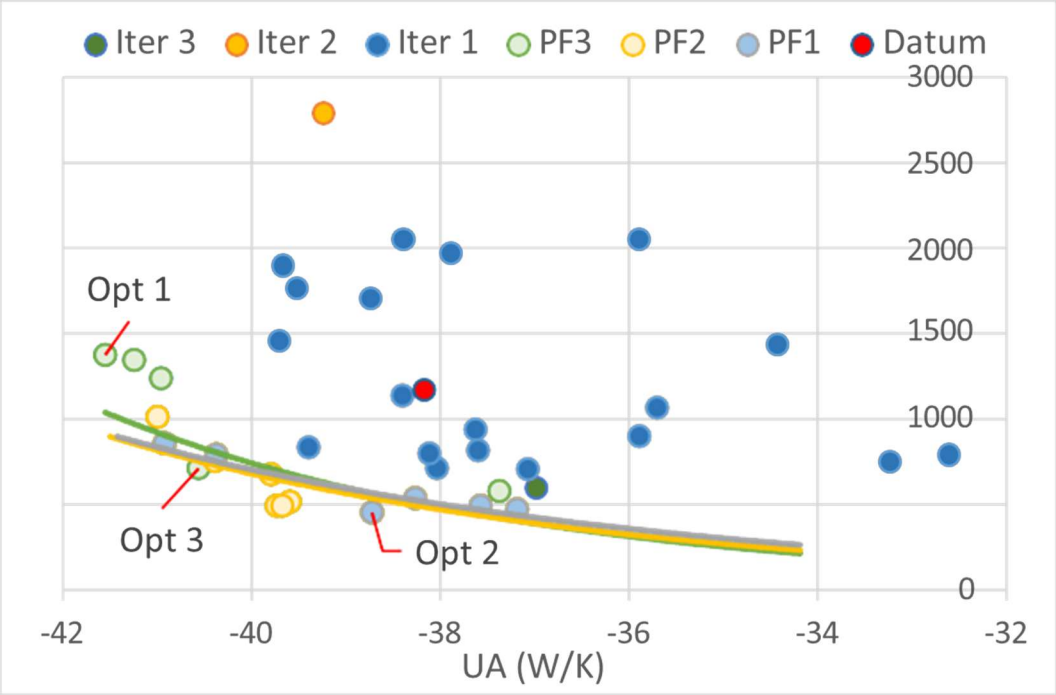

Figure 10: Pareto Fronts History

(a)

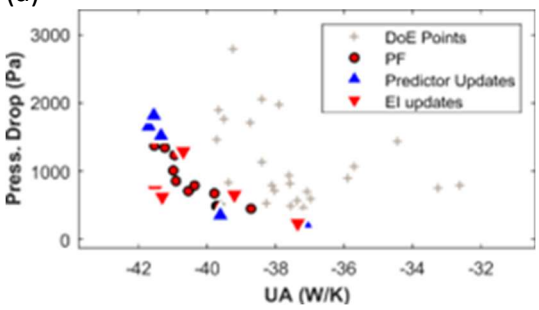

(b)

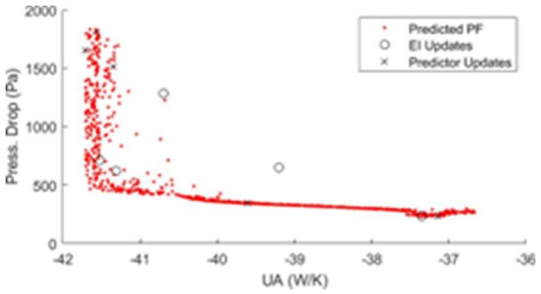

(c)

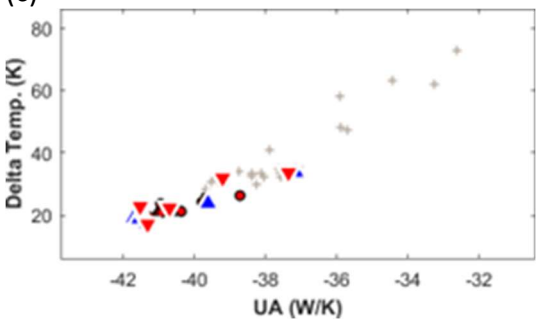

(d)

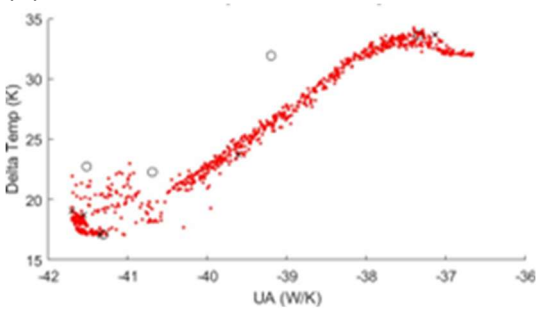

Figure 11: 3rd Iteration Pareto Fronts – UA vs. Pressure drop predicted by optimizer (a) and by CFD (b), UA vs. Delta Temp. predicted by optimizer (c) and by CFD (d)

(a)

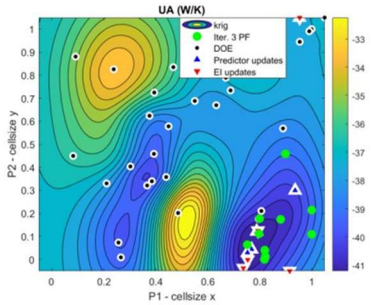

(b)

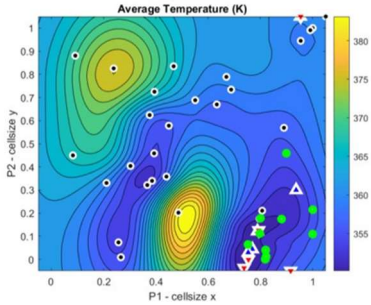

(c)

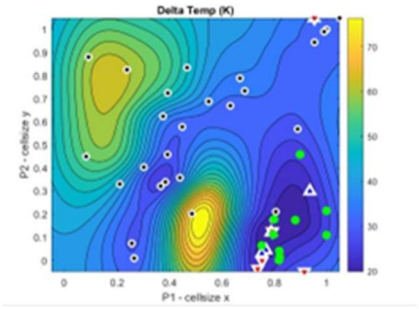

(d)

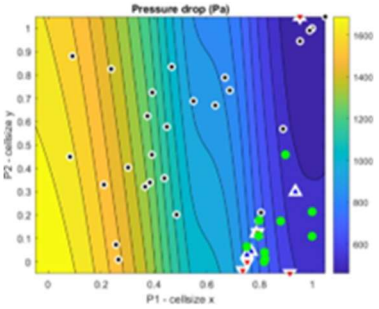

Figure 12: Objectives Cell map for P1 and P2 - the range for P1 and P2 is normalized [0, 1] and includes the 5% design space expansion [-0.05, 1.05].

(a)

(b)

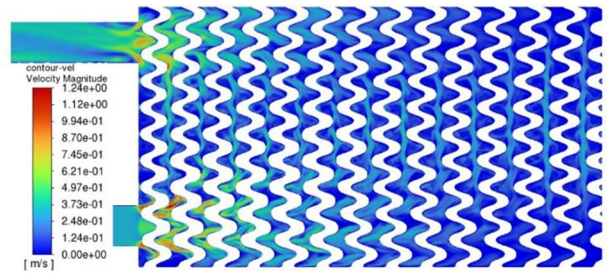

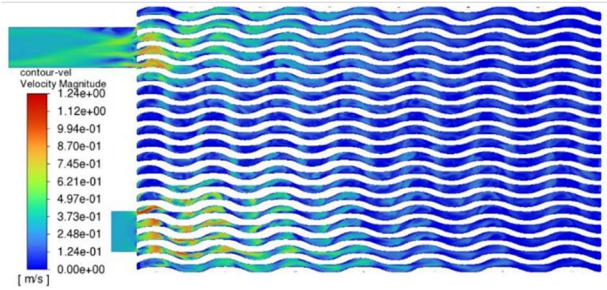

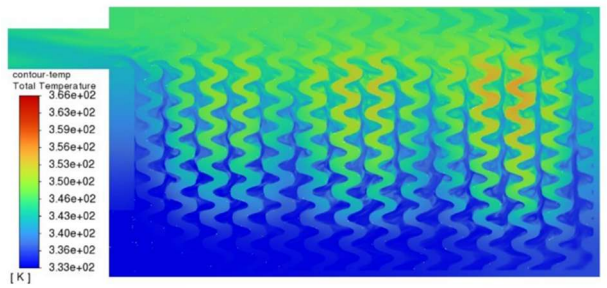

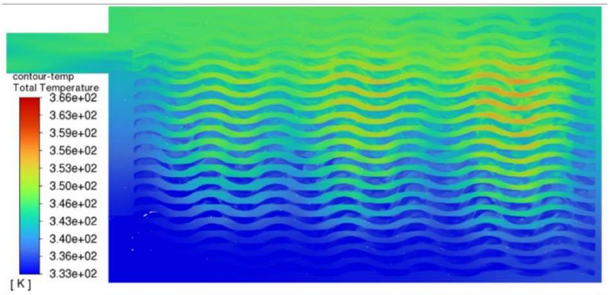

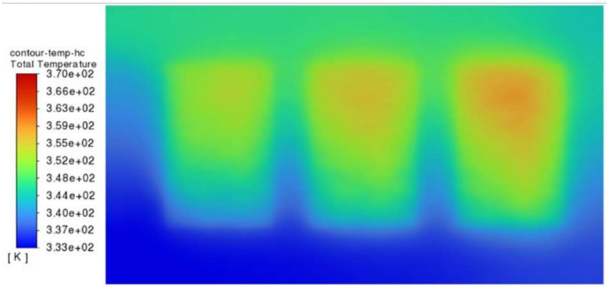

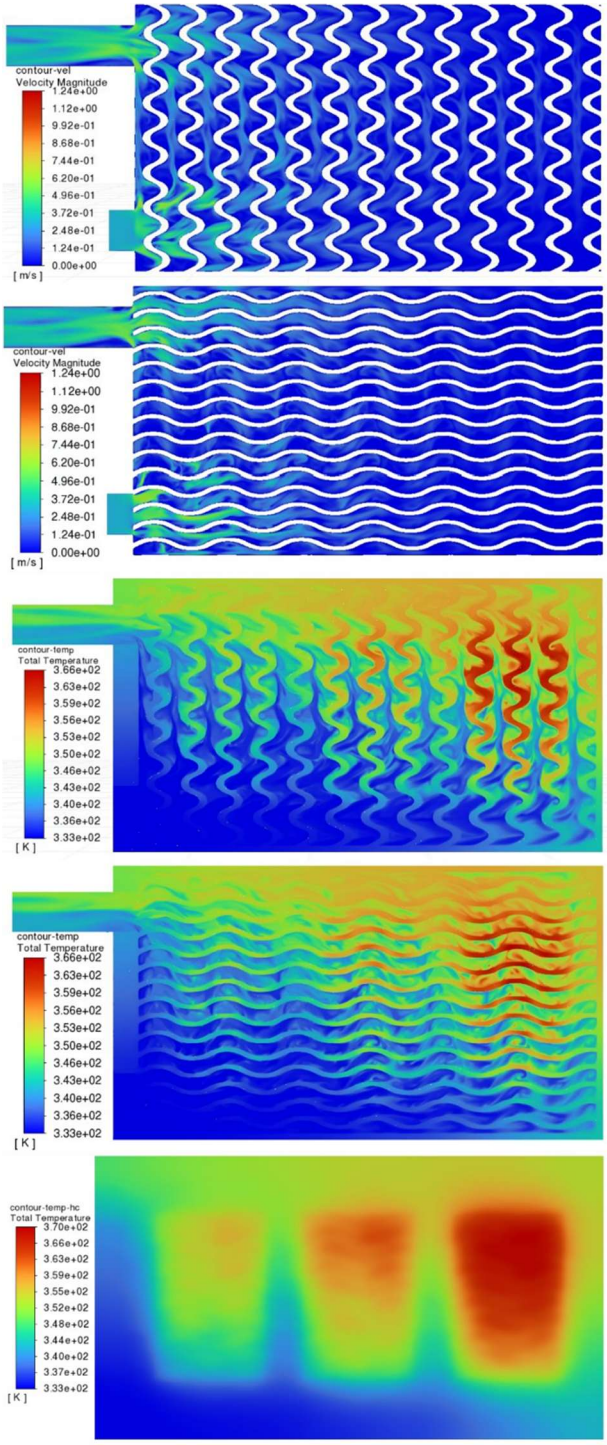

Figure 13: Temp. and Velocity Contours of Opt.1 (a) & Opt. 2 (b)

(a)

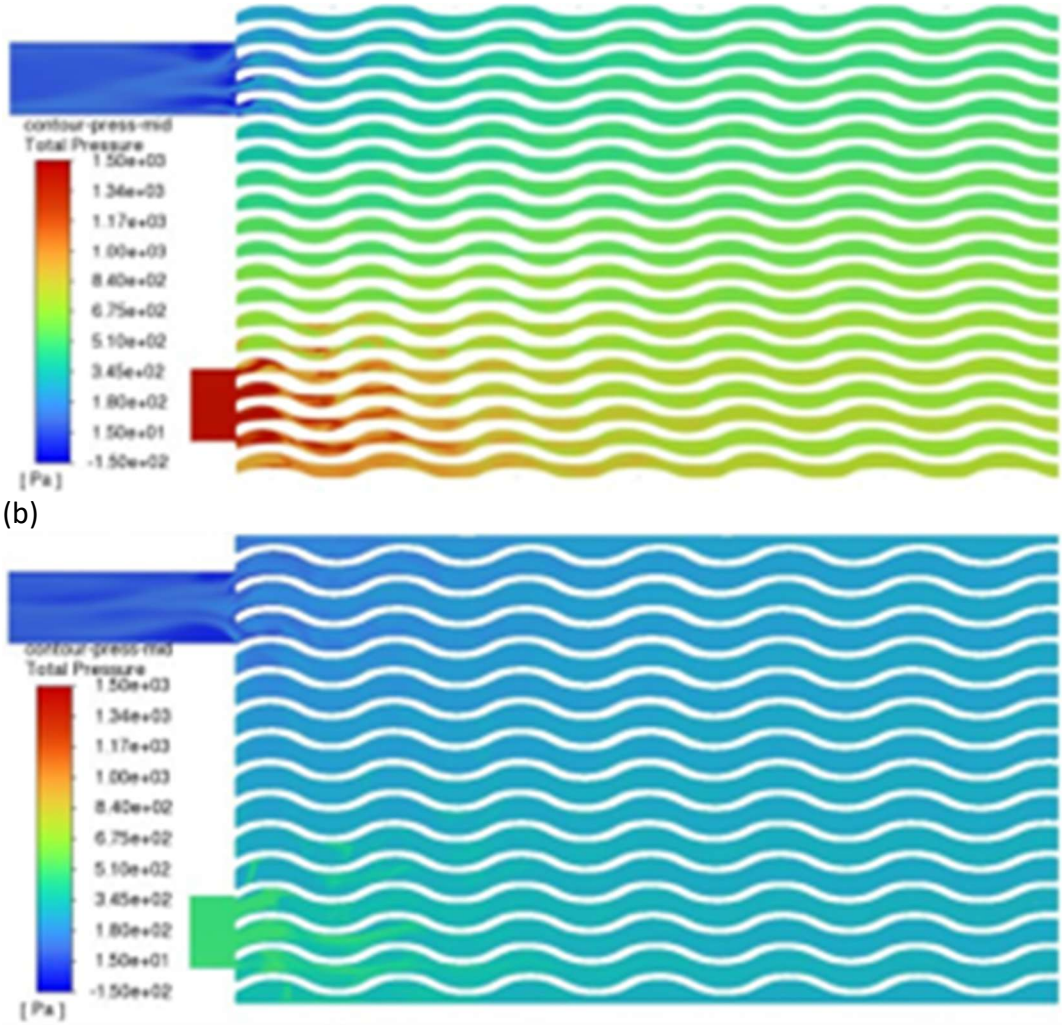

Figure 14: Mid-plane Pressure contours of Opt.1 (a) and Opt.2 (b)

TABLES

ID	Objective	Description
O1.	UA	Effective heat transfer
O2.	T_{avg}	Average temperature for all 6 HC
O3.	ΔT	Maximum temperature difference for the 3rd HC (furthest from inlet)
O4.	ΔP	Surface averaged total pressure difference between inlet and outlet

Table 1: Optimization Objective Functions

ID	Parameter Description	Limits
P1.	Cell size x-axis	[16.2, 37.8] mm
P2.	Cell size y-axis	[13, 21.7] mm
P3.	Scaling factor x-axis	[0, 1]

Table 2: Group 1 Geometric Parameters - Cell Properties

ID	Parameter Description	Limits
P4.	Minimum thickness	[2, 3.5] mm
P5.	Maximum thickness	[3.5, 5] mm

P6.	Plane 1 origin	[-100, 50] mm
P7.	Plane 1 theta	[-90, 90] deg
P8.	Plane 2 origin	[-60, 0] mm
P9.	Plane 2 theta	[-90, 90] deg
P10.	Plane 3 origin	[0, 60] mm
P11.	Plane 3 theta	[-90, 90] deg

Table 3: Group 2 Geometric Parameters - Thickness Variation

Cell Count	U (W/m^2K)	A (m^2)	Press. Drop (Pa)	HC3 delta temp. (K)	Avg. HC temp. (K)
55.6 M	289.33	0.13486	1063.5	33.497	355.86
72.1 M	284.49	0.13489	1127.1	32.296	356.89
85.5 M	282.91	0.13489	1165.8	32.268	357.17
99.3 M	284.38	0.13489	1174.2	31.848	356.89

Table 4: Mesh Dependence Study

Solver	Time	Steady
	Type	Pressure-Based
Viscosity	Model	k-ω SST
Y+	Maximum	2.344
	Average	0.2543

Table 5: CFD Setup

Boundary	*Type*	*Condition*	Units	Value
Heat Cell (x6)	Wall	Heat Flux	W/m^2	94500
Inlet	Mass Flow Inlet	Mass Flow Rate	kg/s	0.05
		Total Temperature	K	333
Outlet	Pressure Outlet	Pressure	Pa	0
		Backflow Total Temperature	K	333
Outer Surface	Wall	Heat Flux	W/m^2	0
Solid Zone	Solid	Thermal Conductivity	W/(m·K)	202.4
		Density	kg/m^3	2719

		Specific Heat	J/(kg·K)	871
Interface	Coupled	Velocity (no-slip)	m/s	0
Fluid Zone	Fluid	Density	kg/m^3	998.2
		Viscosity	kg/(m·s)	0.001003
		Specific Heat	J/(kg·K)	4182
		Thermal Conductivity	W/(m·K)	0.6

Table 6: Boundary Conditions

Iteration	U (W/m^2K)	A (m^2)	Press. drop (Pa)	HC3 delta temp. (K)	Avg. HC temp. (K)
300	289.29	0.13954	786.88	21.172	352.26
500	289.03	0.13954	780.65	21.207	352.35
1000	289.11	0.13954	783.45	21.194	352.34

Table 7: Partial Convergence Study

	Serpentine	Datum	Opt. 1	Opt. 2	Opt. 3
Area Density (m^2/m^3)	68.20	334.11	341.02	363.02	361.38
UA (W/K)	38.88	38.16	41.54	38.72	40.55
$Tavg$ (K)	352.82	357.17	350.00	356.19	352.01
ΔT (K)	11.7	32.27	19.32	26.25	21.33
ΔP (Pa)	14383	1165.8	1370.9	448.74	706.38
Efficiency, %	56.89	94.92	92.26	97.75	95.97
Bulk Reynolds	10617	3561.5	3561.5	3561.5	3561.5
P1	-	27	33.874	35.620	33.905
P2	-	17.35	13.006	16.991	13.354
Aspect Ratio	-	1.556	2.604	2.096	2.539
P3	-	0	0.549	0.248	0.105
P4	-	3.5	3.524	2.592	2.973
P5	-	3.5	4.451	3.706	4.596
P6	-	-	39.789	14.220	50.000
P7	-	-	-50.777	-46.239	-49.397
P8	-	-	0.000	30.826	0.000
P9	-	-	99.000	-17.339	-90.000
P10	-	-	90.000	-66.881	90.000
P11	-	-	59.039	-66.881	-82.053

Table 8: Optimum Designs Results Comparison and Parameters

		Serpentine		Opt.1	
	Original	High $\dot{m}$	Original	High $\dot{m}$	Low Tin
$\dot{m}$ (kg/s)	0.05	0.1	0.05	0.1	0.05
Tin (K)	333	333	333	333	288.15
UA (W/K)	38.88	44.54	41.54	45.32	269.14
$Tavg$ (K)	352.82	341.00	350.00	344.09	305.20
ΔT (K)	11.7	7.98	19.32	12.81	19.58
ΔP (Pa)	14383	48824	1370.9	4603.7	1370.8
Efficiency, %	56.89	8.27	92.26	55.87	-

Bulk Reynolds	10617	21157	3561.5	7122.9	3561.5

Table 9: Opt.1 Design Robustness